Radiative damping and synchronization in a graphene-based terahertz emitter

A. S. Moskalenko and S. A. Mikhailov

Citation: Journal of Applied Physics **115**, 203110 (2014); doi: 10.1063/1.4879901
View online: http://dx.doi.org/10.1063/1.4879901
View Table of Contents: http://scitation.aip.org/content/aip/journal/jap/115/20?ver=pdfcov
Published by the AIP Publishing

Radiative damping and synchronization in a graphene-based terahertz emitter

A. S. Moskalenko[a] and S. A. Mikhailov[b]
Institute of Physics, University of Augsburg, D-86135 Augsburg, Germany

(Received 10 April 2014; accepted 14 May 2014; published online 29 May 2014)

We investigate the collective electron dynamics in a recently proposed graphene-based terahertz emitter under the influence of the radiative damping effect, which is included self-consistently in a molecular dynamics approach. We show that under appropriate conditions synchronization of the dynamics of single electrons takes place, leading to a rise of the oscillating component of the charge current. The synchronization time depends dramatically on the applied dc electric field and electron scattering rate and is roughly inversely proportional to the radiative damping rate that is determined by the carrier concentration and the geometrical parameters of the device. The emission spectra in the synchronized state, determined by the oscillating current component, are analyzed. The effective generation of higher harmonics for large values of the radiative damping strength is demonstrated. © *2014 AIP Publishing LLC*. [http://dx.doi.org/10.1063/1.4879901]

I. INTRODUCTION

The electromagnetic radiation of terahertz frequencies ($0.1 \lesssim \nu \lesssim 10\,\mathrm{THz}$) has many potential applications in medical imaging, security, astronomy, and other areas. The sources of coherent and powerful THz radiation are, however, mainly restricted to vacuum devices like backward wave oscillators or free electron lasers. The operation principle of these devices is based on the Smith-Purcell effect:[1] electromagnetic waves are emitted by a fast electron beam moving across a periodic potential. The radiation frequency of the Smith-Purcell emission

$$\nu_{\mathrm{SP}} = \frac{v_0}{a_x} \tag{1}$$

is determined by the drift velocity of the electrons v_0 and the period of the potential a_x. It can be controlled by a dc voltage which accelerates electrons up to the velocity v_0.

The vacuum devices are bulky and expensive. The need for a compact source of terahertz radiation stimulated experiments (e.g., Refs. 2–4) attempting to create a solid-state Smith-Purcell emitter. In such experiments, semiconductor structures, like GaAs/AlGaAs quantum wells, have been used, with a metallic grating evaporated on top of the system. Electrons were driven in a two-dimensional (2D) channel in the direction perpendicular to the grating stripes, but instead of the coherent Smith-Purcell emission with the velocity-dependent frequency (1) a weak thermal radiation at the frequency of 2D plasmons $\nu_{\mathrm{p}} = \omega_{\mathrm{p}}/2\pi$ was observed. The reason for this failure was clarified in Ref. 5. It was shown that the strong coherent radiation is observed at the frequency (1) only if the drift velocity v_0 substantially exceeds a threshold value

$$v_0 \gg v_{\mathrm{th}} \simeq \nu_{\mathrm{p}} a_x = \sqrt{\frac{n_{\mathrm{s}} e^2 a_x}{m\epsilon}}, \tag{2}$$

where e, m, and n_{s} are the charge, the effective mass, and the 2D density of electrons and ϵ is the dielectric permittivity of the surrounding medium. In vacuum devices, the condition (2) is easily satisfied, but in semiconductors the plasma frequency is very large so that typically the relation $v_0 \ll v_{\mathrm{th}}$ holds. In this case, however, the system emits at the plasma frequency ν_{p} due to the heating of the electron gas (the thermal radiation). As seen from Eq. (2), the Smith-Purcell emission can be realized if a small amount of electrons can be driven with a sufficiently large velocity.

The discovery of graphene[6–8] opened great opportunities in exploring unique properties of this material in scientific research and practical applications. Recently, it was shown[9] that, due to the massless energy dispersion and the very large Fermi velocity of graphene electrons (as compared to semiconductors), the Smith-Purcell emission condition (2) can be realized in graphene. A specific device structure proposed in Ref. 9 consists of two graphene layers lying on a substrate and separated by a thin boron-nitride (BN) dielectric (see Fig. 1). The first graphene layer (Fig. 1(b)) has the form of an array of narrow stripes oriented along the x-axis. The second graphene layer (the gate, Fig. 1(c)) consists of a set of perpendicular stripes with the period a_x and serves as a grating coupler. A strong dc current is driven in the first (active) layer from the left (source) to the right (drain) contact, and the periodic potential is produced by applying a weak dc voltage between the two graphene layers. The calculations of Ref. 9 showed that the proposed structure should be able to coherently emit at frequencies ranging from fractions of terahertz up to $\simeq$30 THz with the power density up to 0.5 W/cm^2.

The theory of Ref. 9 is based on a single-particle approach which corresponds to the cold plasma approximation. In such an approach, one considers the motion of a single particle under the action of the driving dc electric field

[a]Also at Ioffe Physical-Technical Institute of RAS, 194021 St. Petersburg, Russia. Electronic mail: andrey.moskalenko@physik.uni-augsburg.de.
[b]Email: sergey.mikhailov@physik.uni-augsburg.de

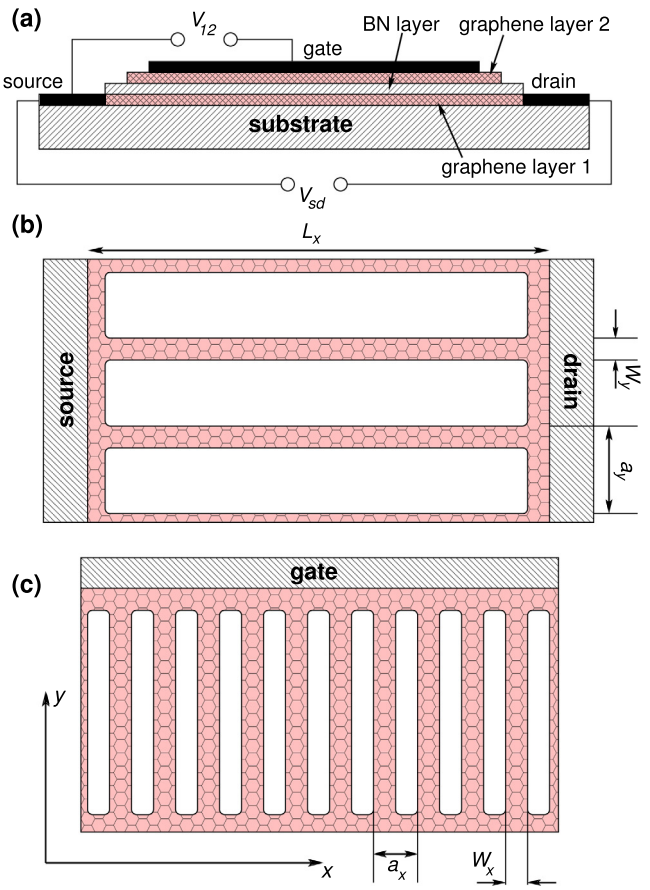

FIG. 1. The geometry of the device: (a) the side view, (b) the top view of the first (active) graphene layer, (c) the top view of the second graphene layer. The first graphene layer lying on the dielectric substrate has the form of an array of stripes with the width W_y and the period a_y. The second layer (the gate) serves as a grating with the stripe width W_x and the period a_x. The layers are separated by a thin dielectric (e.g., BN) of thickness d. In the operation mode, a large (driving) dc voltage V_{sd} is applied between the source and drain and a weak dc voltage V_{12} creating the periodic potential (3) is applied between the gate and the first graphene layer. The length of the sample in the x-direction is L.

and the periodic potential and ignores the thermal (or Fermi) distribution of electrons over quantum states. In this paper, we treat the problem within the molecular dynamics approach, taking into account the electron statistics as well as the back action of the emitted radiation to the electron dynamics in the structure. Starting from a homogeneous thermal distribution at the applied dc electric field, we analyze the nonlinear dynamics of the electron momentum and coordinate distributions, as well as the resulting current density dynamics, after the periodic potential is switched on. We demonstrate how the back action of the radiation synchronizes the oscillatory motion of electrons and stimulates all electrons to emit coherently. The synchronization of the electron motion (the radiative damping) is a prerequisite for an effective emission from the device; therefore, the understanding of the studied processes is important for the efficient device operation.

The synchronization itself is an interesting phenomenon in nonlinear science which was widely studied in physical, chemical, biological, and social systems.[10–12] Typically, the synchronization occurs on a much longer time scale than the characteristic time scales of single oscillators. The onset of the synchronization and the dynamics of the order parameters characterizing the synchronization belong to open general problems in nonlinear science.[13] In this work, we address these problems numerically in the particular case of the electron dynamics in the proposed graphene-based terahertz emitter.

II. THEORETICAL MODEL

Following Ref. 9, we consider the motion of electrons in graphene stripes of the first layer (Fig. 1) under the action of the dc electric field $E_0 = V_{sd}/L$ and the periodic potential $U(x)$ created by the voltage V_{12} between the layers. The spectrum of electrons in the stripes has the form $E_{\pm,n}(p) = \pm\sqrt{\Delta_0^2 n^2 + v_F^2 p^2}$ (see inset of Fig. 2), where $n = 1, 2, \ldots$. The gap at the Dirac point $2\Delta_0$ is assured by an appropriate choice of the stripe boundary conditions and is of the order of $\pi\hbar v_F/W_y$,[9,14–16] where v_F is the Fermi velocity in the bulk graphene. The periodic potential seen by electrons of the main layer is modeled as

$$U(x) = U_0 \frac{\tanh[S\sin(2\pi x/a_x)]}{\tanh S}, \tag{3}$$

where U_0 and a_x are the amplitude and the period of the potential, and the parameter S characterizes its steepness: at $S \ll 1$, the potential is practically sinusoidal, whereas at $S \gg 1$ it has a periodic rectangular shape and contains many spatial Fourier harmonics. In the experiment, the strongly non-sinusoidal regime $S \gg 1$ is realized if the distance d between the main and the grating graphene layers is much smaller than the grating period a_x (for example, if the BN dielectric layer between the graphene sheets is about 5–10 nm, while the grating period exceeds 0.1–1 μm). The total potential seen by the electrons in the graphene stripes is shown in Fig. 2.

In order to model the dynamics of electrons, we apply a molecular dynamics approach and describe it by the following equations of motions:

$$\frac{dx_i}{dt} = v_i = \frac{v_F^2 p_i}{\sqrt{\Delta_0^2 + v_F^2 p_i^2}}, \quad i = 1, 2, \ldots, N, \tag{4}$$

$$\frac{dp_i}{dt} = -\gamma p_i - eE_0 - \frac{dU(x_i)}{dx_i} - eE_{ac}(t). \tag{5}$$

Here, $-e$, x_i, p_i, and v_i are the charge, coordinate, momentum, and velocity of the ith electron, respectively, whereby the total number of electrons in an ensemble of the parallel stripes amounts to N. The first term on the right hand side of Eq. (5) accounts for the relaxation processes, whereby γ is the phenomenological scattering rate. The physical meaning of the last term in Eq. (5) can be explained as follows. If the periodic potential is absent and electrons move only under the action of the dc electric field E_0, their velocity v_i and the total current

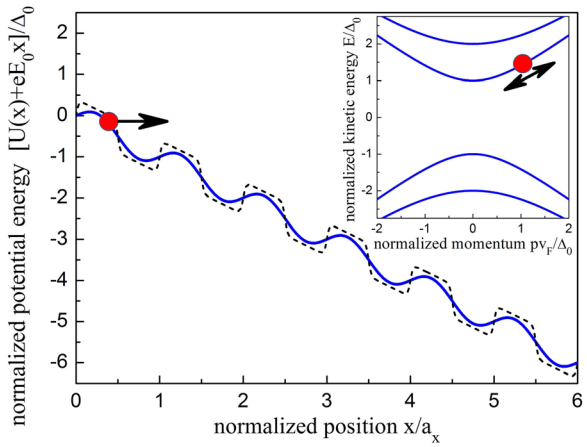

FIG. 2. Electron moving in a total potential $U(x)+eE_0x$ created by the periodic potential (3) and the dc driving field E_0. For this illustration, we selected the value of the applied dc electric field such that $-eE_0a_x/\Delta_0 = 1$, whereas $U(x)$ is determined by Eq. (3) with $S = 0.1$ and $U_0/\Delta_0 = 0.3$ (solid blue line) and $S = 5$ and $U_0/\Delta_0 = 0.4$ (dashed black line). Inset illustrates the energy band structure of a graphene stripe and the variations of the electron kinetic energy in the first conduction subband.

$$j_x = -en_s\frac{1}{N}\sum_{i=1}^{N} v_i = -en_s\frac{1}{N}\sum_{i=1}^{N}\frac{v_F^2 p_i}{\sqrt{\Delta_0^2 + v_F^2 p_i^2}}, \qquad (6)$$

are time-independent, and the ac electric field $E_{ac}(t)$ is zero. Here, n_s denotes the average two-dimensional electron density. If the potential $U(x)$ is switched on, electrons moving across this potential with a large average velocity v_0 begin to oscillate in time, and hence, to emit electromagnetic waves. The electric $E_x(z,t)$ and magnetic $B_y(z,t)$ fields of this wave are proportional to $e^{i\omega|z|/c-i\omega t}$, where c is the light velocity and ω is the frequency of the emitted radiation. The force $-eE_{ac}(t)$ in Eq. (5) is due to this field at $z = 0$, $E_{ac}(t) \equiv E_x(0,t)$; it describes the back influence of the radiation on the electron dynamics and works as an additional friction force (the radiative damping).

The field $E_{ac}(t)$ is related to the current density (6) by the Maxwell equations. In the Appendix, we show that $E_{ac}(t)$ can be written as

$$E_{ac}(t) = -\frac{2\pi}{c}\left[j_x(t) - \bar{j}_x(t)\right], \qquad (7)$$

where

$$\bar{j}_x(t) = \gamma_L\int_{-\infty}^{t} j_x(t')\exp[-\gamma_L(t-t')]\mathrm{d}t', \qquad (8)$$

and the cut-off parameter

$$\gamma_L = \frac{2\pi c}{L} \qquad (9)$$

is related to the length of the sample. The correction $\bar{j}_x(t)$ ensures that low frequency components of E_{ac} with $\omega \ll \gamma_L$ vanish because in this case the radiation wavelength λ is much larger than the length of the sample L. At high frequencies $\omega \gg \gamma_L$, the correction $\bar{j}_x(t)$ reduces to an average dc current at the time moment t, which does not contribute to the emission and therefore to the radiative damping. Up to this shift the term $-eE_{ac}$ in Eq. (5) is then of the order $-\Gamma\sum_{i=1}^{N} p_i/N$, where Γ is the characteristic radiative-damping rate[17] of a single (free-standing) layer

$$\Gamma = \frac{2\pi n_s e^2 v_F^2}{\Delta_0 c}. \qquad (10)$$

It will be seen below that the synchronization time decreases and the efficiency of the coherent radiation increases if the radiative-damping parameter Γ is large. It cannot, however, be sufficiently enlarged solely by the increase of the electron density n_s since then the plasma frequency ν_p increases too and this starts to contradict to the threshold condition (2). This difficulty can be overcome by placing the graphene emitter in a cavity (e.g., between THz mirrors[18]). Then, the radiative damping Γ can be significantly increased independent of the plasma frequency. Below we will treat Γ as a parameter which can be varied independently of n_s and ν_p. This model for the radiative damping term E_{ac} is well applicable and is insensitive to the choice of L if the condition $2\pi\nu_0 \gg \gamma_L$ is fulfilled, where

$$\nu_0 = v_F/a_x. \qquad (11)$$

Using Eq. (9), we get then a restriction for the sample length $L \gg \lambda_0$, where λ_0 is the characteristic radiation wavelength. For the grating period $a_x \sim 0.5 - 5\,\mu$m, we have $\nu_0 \sim 1 - 10\,$THz ($\lambda_0 \sim 0.3 - 0.03\,$mm), so that the sample should be longer than ~1–0.1 mm.

The system of equations to be solved is thus given by Eqs. (4)–(8). Notice that the radiative damping term $-eE_{ac}$, which is given by the sum over i and thus proportional to the current of *all* particles (6), leads to a coupling of the single-particle Eqs. (4) and (5) for different i. This leads to a synchronization of the electron dynamics: while just after the potential $U(x)$ is switched on all electrons oscillate with different phases (incoherent emission), after a while their phases become synchronized due to the radiative damping coupling, and the emission becomes coherent. As will be seen below, the synchronization time τ_{sync} is governed by the ratio Γ/ν_0. The typical value of $\Gamma/2\pi$ calculated from Eq. (10) lies between 0.1 and 1 THz (cf. Ref. 17) and can be much larger if THz mirrors are used[18] (for comparison, as mentioned, ν_0 is in the range of 1–10 THz).

III. SIMULATION RESULTS

In simulations presented below, we fixed the periodic potential amplitude U_0 to $U_0/\Delta_0 = 0.3$ and assume that only the lowest electron energy band is populated. The calculations were performed with $N = 10^6$ electrons; the further increase of N practically did not change the results. The cut-off parameter was chosen to be $\gamma_L = \nu_0$ which corresponds to the device length $L \approx 2 \times 10^3 a_x$, but the results were found to be insensitive to γ_L if it was varied from $0.1\nu_0$ to $2\nu_0$.

Figure 3(a) shows the time dynamics of the generated charge current at different values of the applied dc electric field E_0. Initially, at $t < 0$, the periodic grating potential is

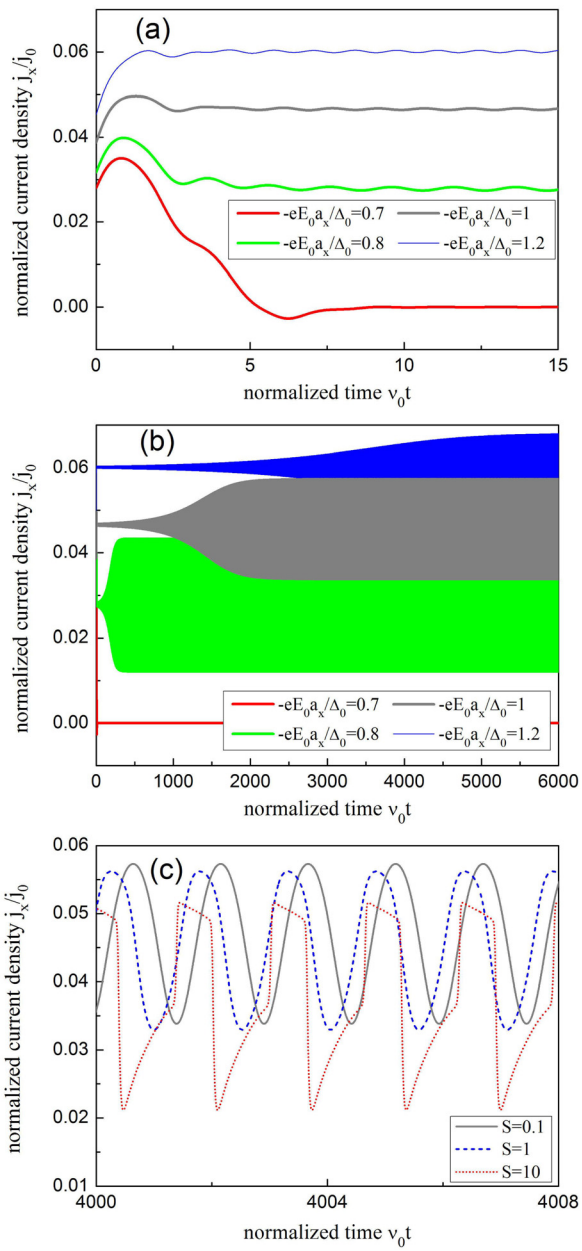

FIG. 3. (a) Time dependence of the charge current density at a short time scale for different values of the applied dc electric field E_0. Values of E_0 shown in the legend increase for the curves from the bottom to the top of the figure. Other parameters of the simulations: $S = 0.1$, $\Gamma/\nu_0 = 0.1$, and $\gamma/\nu_0 = 1$. The current density is normalized by $j_0 = -en_s v_F$. (b) The same dynamics is shown at a long time scale. (c) Dependence of the current density oscillations on the periodic potential steepness parameter S. The oscillations are shown in the correspondingly short time interval when they have stabilized. Other parameters of the simulations: $-eE_0a_x/\Delta_0 = 1$ in (c), $\Gamma/\nu_0 = 0.1$, and $\gamma/\nu_0 = 1$.

switched off. The electrons move in the potential of the dc field. They have a homogeneous spatial distribution whereas their concentration is low enough so that their momenta obey a Boltzmann distribution at temperature $T = 1.2\Delta_0$ shifted by the applied dc electric field (the condition $T = 1.2\Delta_0$ corresponds to $T = 300\,\mathrm{K}$ for $W_y = 0.1\,\mu\mathrm{m}$). At $t = 0$, the periodic grating potential is switched on. At first, this leads to a quick redistribution of the electrons, which can be observed in the charge current dynamics as oscillations relaxing at the time scale of the order of $1/\gamma$ (see Fig. 3(a)). The charge current dynamics at a longer time scale is presented in Fig. 3(b). We see that for small values of E_0 the system arrives, after the short period of relaxation, to a state with no flowing current. An increase of the dc electric field leads to a change in the current dynamics: a dc current, along with an initially small ac current component, appears. The oscillation amplitude of the ac contribution increases with time and finally saturates. The stabilization time of the current dynamics is much longer than the initial relaxation time and the period of the current oscillations; therefore, they are not resolved in Fig. 3(b).

The stabilization time strongly depends on the value of the applied dc electric field. As seen from Fig. 3(b), a relatively small increase of this value leads to a dramatic growth of the time required for the stabilization of the current oscillations. The increase of the dc electric field leads also to an increase of the dc current component. On the contrary, the amplitude of the stabilized ac current oscillations moderately decreases. These oscillations are resolved in Fig. 3(c), where they are shown at different values of the steepness parameter S. As it was already discussed in Ref. 9, for small values of S, i.e., $S \ll 1$, the oscillations are essentially harmonic whereas for $S \gg 1$ the anharmonicity becomes strongly pronounced.

In order to understand the observed behavior of the current, and specifically the rise of its oscillations in time with the subsequent stabilization, we have analyzed the dynamics of the coordinate and momentum distributions in the system. The snapshots of the momentum distribution, corresponding to the current dynamics shown in Fig. 3(b) for $-eE_0a_x/\Delta_0 = 1$ (gray curve in Fig. 3(b)), are presented in Fig. 4. The snapshots of the spatial distribution for the same simulation are shown in Fig. 5. The first snapshots at $\nu_0 t = 200$ are taken already well after the short initial stage of the current relaxation. From the momentum distribution (Fig. 4(a)), we see that a part of the electrons stopped whereas another part is distributed in some momentum range. The coordinate distribution (Fig. 5(a)) shows periodic peaks with the period of the lattice potential a_x. These peaks are positioned at local minima of the total potential energy, formed by the periodic lattice potential and the potential of the applied dc electric field (cf. Fig. 2). It is clear that if the dc electric field is chosen to be large enough, the local minima of the potential energy no longer exist and the electrons cannot be captured. Once captured, such electrons do not influence the dynamics of the moving electrons.

The electrons which are not captured by the potential minima at $\nu_0 t = 200$ are distributed already not completely homogeneously but still quite evenly in space (see Fig. 5(a)). Actually, on a short time scale, comprising however tens of oscillations periods, all of them have the same periodic dynamics and oscillate in momentum space between the upper and lower bounds which are strongly pronounced in Fig. 4(a) (and later in Figs. 4(b) and 4(c)). The difference between the electrons, leading to their distribution in space and momentum, comes from their different phases. At the initial stage, the phases are determined by the initial conditions and the short relaxation stage in the beginning. The interaction between the electrons via the radiative damping

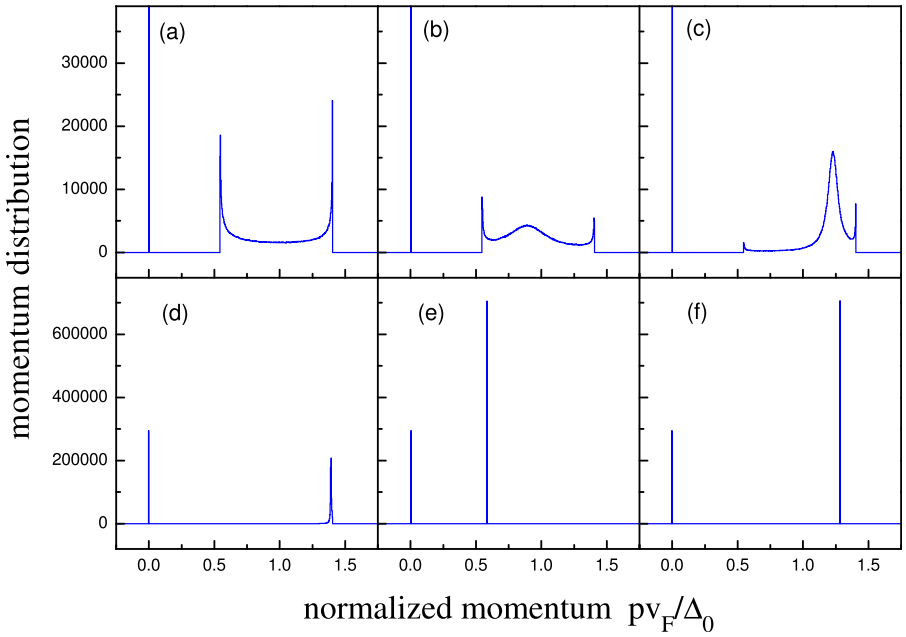

FIG. 4. Snapshots of the momentum distribution at different time moments: (a) $\nu_0 t = 200$, (b) $\nu_0 t = 1500$, (c) $\nu_0 t = 1800$, (d) $\nu_0 t = 2100$, (e) $\nu_0 t = 4000$, and (f) $\nu_0 t = 5000$. Parameters of the simulation are the same as for the gray curve in Fig. 3: $-eE_0 a_x/\Delta_0 = 1$, $S = 0.1$, $\Gamma/\nu_0 = 0.1$, and $\gamma/\nu_0 = 1$.

term leads to adiabatic changes of these phases. The electrons feel each other and start to synchronize their motion.

At $\nu_0 t = 1500$ (see Figs. 4(b) and 5(b)), the synchronization is already distinguishable. We see that in both distributions moving electrons group together forming oscillating humps. Then between $\nu_0 t = 1800$ and $\nu_0 t = 2100$ (see Figs. 4(c), 4(d), 5(c), and 5(d)) the synchronization becomes strongly pronounced. At $\nu_0 t = 4000$ and $\nu_0 t = 5000$ (see Figs. 4(e), 4(f), 5(e), and 5(f)), all moving particles have practically the same phase. Therefore, all of them have practically the same momentum, which oscillates between the same lower and upper bounds. In the coordinate space, the electrons cluster in separate bunches, like in the case of the synchrotron radiation,[19] which move through the periodic potential with a constant and a periodically oscillating components of the velocity. The distance between the bunches amounts to exactly the period of the lattice potential a_x. The width of the bunches, both in the momentum and coordinate spaces, tends to zero with time.[20] Thus, in the synchronized state, the dynamics of all the electrons is similar to the electron dynamics in the single-electron model[9] but with an additional nonlinear decay term corresponding to the radiative damping. In the case of a relatively small radiative-damping rate Γ, $\Gamma \ll \gamma$, the amplitude of the oscillating current component in the synchronized state is approximately proportional to the electron density. From Fig. 3(b), we can see that this amplitude depends on the applied dc electric field E_0.

For small values of E_0, the electrons move so slowly that they lose more energy due to the relaxation as they move between two neighboring local maxima of the total potential (cf. Fig. 2) than the difference in energy between these two maxima. Therefore, independent of the initial

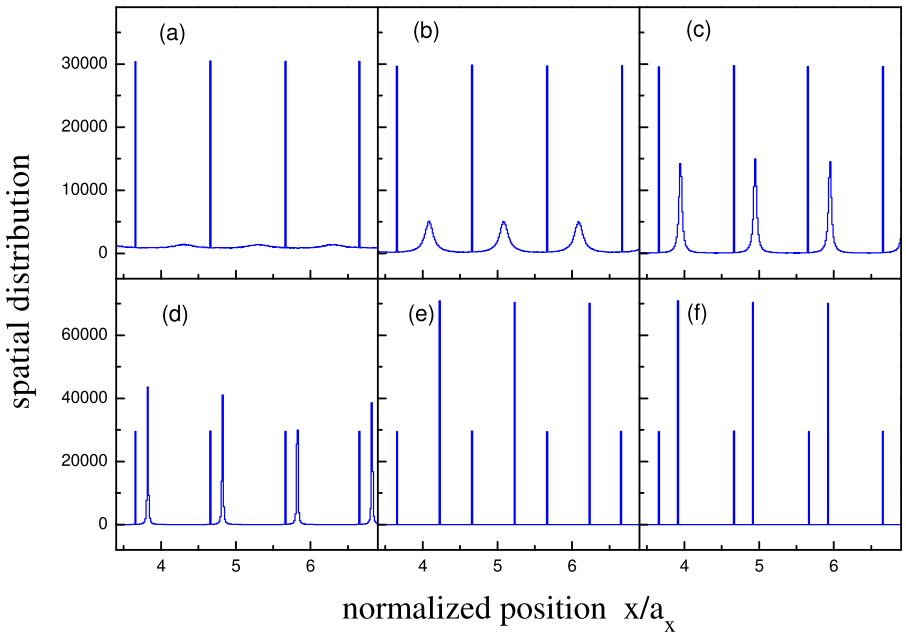

FIG. 5. Snapshots of the spatial distribution at different time moments: (a) $\nu_0 t = 200$, (b) $\nu_0 t = 1500$, (c) $\nu_0 t = 1800$, (d) $\nu_0 t = 2100$, (e) $\nu_0 t = 4000$, and (f) $\nu_0 t = 5000$. Parameters of the simulation are the same as in Fig. 4. Note that the vertical scale is different for figures (a)–(c) and (d)–(f). The peaks having the same positions in all the figures correspond to the electrons captured by the local minima of the total potential energy profile. The other distribution peaks, which build up with time due to the synchronization of the electron motion, move unidirectionally, whereas their velocity oscillates periodically (cf. Fig. 4).

conditions, at some moment they cannot overcome the next potential barrier and relax to a local minimum of the potential. An increase of E_0 leads to a situation when two possible types of trajectories in the phase space become possible: bound and unbound. Depending on initial conditions, each electron can either relax to one of the local potential minima or to propagate in space so that the energy lost in the course of motion between two local potential maxima is compensated by the energy difference in the height of these maxima. The larger the value of the applied dc electric field, the less is the number of electrons captured by the local minima of the potential. There is a very narrow range of the dc electric field values, where this effect leads to a rapid increase of the oscillation amplitude of the stabilized current with E_0. Then, as seen from Fig. 3(b), the amplitude of the stationary current oscillations starts to drop with the increase of E_0. Further increase of the applied dc electric field leads to a situation when there are no local minima of the potential and all electrons follow unbound trajectories in the phase space. The current oscillation amplitudes continue to decrease with the growth of E_0, since the kinetic energy gained by the electrons increases as compared to their potential energy determined by the periodic potential. Also the synchronization time τ_{sync} increases dramatically with the increase of E_0. Thus, for a realization of a coherent emission, there is a range for optimum dc electric field values.

In Fig. 6, we illustrate the charge current dynamics in the system at different values of the damping parameters γ and Γ. Figure 6(a) shows that the influence of the scattering relaxation rate γ on the current oscillations is opposite to that of the dc electric field E_0. This refers both to τ_{sync} and to the current oscillation amplitude. It is the ratio between E_0 and γ, which mostly determines the final average electron velocity in the system, that is crucial for the system dynamics and the properties of the generated ac current.

Figure 6(b) shows that an increase of the radiative damping rate Γ reduces the synchronization time τ_{sync}. The time τ_{sync} is roughly inversely proportional to Γ and saturates at $\Gamma/\nu_0 \gtrsim 1$, where we have also $\Gamma \gtrsim \gamma$. For small values of Γ, the radiative damping term does not influence the single electron dynamics on a short time scale ($\Delta t \sim 1/\nu_0$) leading only to adiabatic changes of their phase in time. The rate of these changes is proportional to Γ. For large values of Γ also the single electron dynamics on a short time scale, including the initial relaxation process, is strongly influenced by the radiative damping because in this regime the radiative damping term is of the same order or larger than the scattering term $-\gamma p_i$ in Eq. (5)

Another interesting feature observed for large values of Γ is an appearance of a pronounced anharmonicity of the stabilized current oscillations (see inset of Fig. 6(b)) like in the case of the large values of the steepness parameter S of the periodic potential (cf. Fig. 3(c)). This is again a consequence of the fact that the dynamics on a short time scale becomes strongly affected by the radiative damping. The anharmonicity of the charge current oscillations is reflected in the corresponding emission spectra.

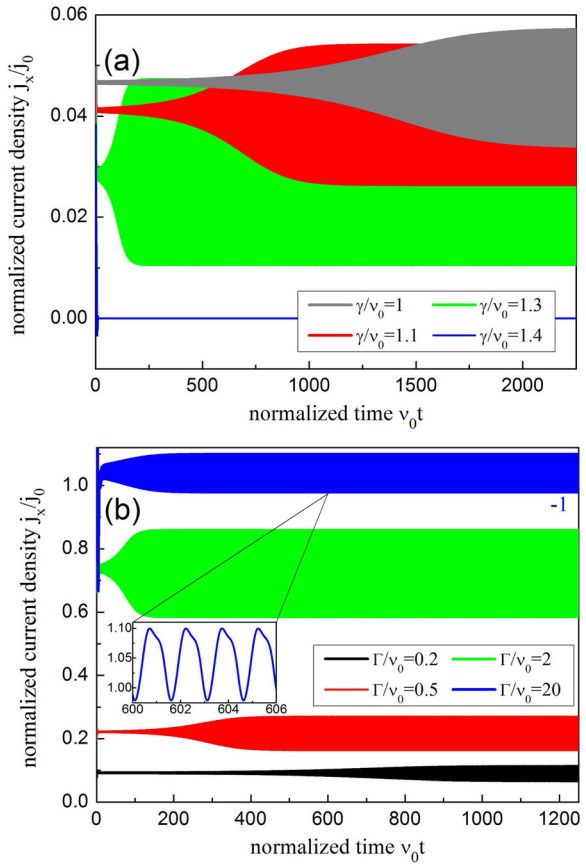

FIG. 6. (a) Current density dynamics for different values of the phenomenological scattering rate γ. Values of γ shown in the legend increase for the curves from the top to the bottom of the figure. Other parameters of the simulations: $-eE_0a_x/\Delta_0 = 1$, $S = 0.1$, and $\Gamma/\nu_0 = 0.1$. (b) Current density dynamics for different values of the radiative damping rate Γ. Values of Γ shown in the legend increase for the curves from the bottom to the top of the figure. For better readability of the figure, the upper curve for $\Gamma/\nu_0 = 20$ is offset by -1 that is indicated by the corresponding number in the figure. Other parameters of the simulations: $-eE_0a_x/\Delta_0 = 1$, $S = 0.1$, and $\gamma/\nu_0 = 1$. Inset shows the short-time current dynamics in the synchronized state for $\Gamma/\nu_0 = 20$.

The current oscillations discussed above result in the radiation of the electromagnetic waves. The spectra of this radiation were calculated applying the theory of the time-dependent emission spectra,[21–23] whereby a time detection window ΔT covering several oscillation periods was used. Figure 7 illustrates the emission spectra calculated in the synchronized state, when the spectra become independent of time. In Fig. 7(a), the emission spectra are presented for several values of the applied dc electric field corresponding to Fig. 3(b). We see that the main emission frequency increases with the dc electric field and is roughly proportional to it. The main reason for this behavior is that the main emission frequency is determined by the final average electron velocity,[9] which increases with the electric field. Analogously, larger relaxation rates γ lead to smaller emission frequencies (not shown here). For small values of S and Γ, the charge current oscillations are almost harmonic. Therefore, high harmonics in the spectra are weak. Their strength rises slightly in respect to the main harmonic when the dc electric field increases. Higher harmonics become pronounced in case of large values of S, as it was shown in the framework

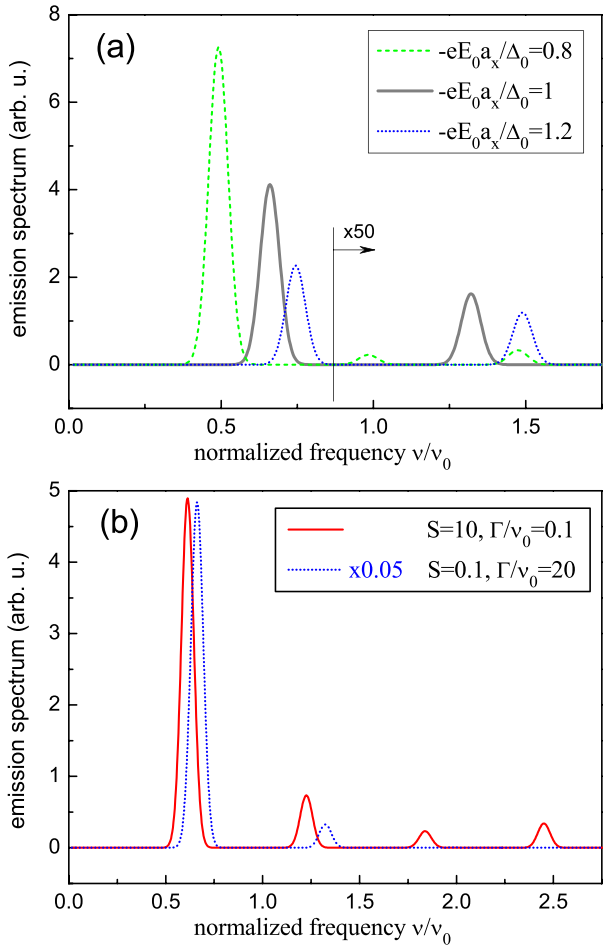

FIG. 7. (a) Emission spectra in the synchronized phase for different values of the applied dc electric field E_0, corresponding to Fig. 3(b), where $S = 0.1$. To the right of the black vertical line, the spectra are multiplied by the factor 50. (b) Emission spectra in the synchronized phase with pronounced high harmonics for large values of the potential steepness parameter S or the radiative damping rate Γ, with $-eE_0a_x/\Delta_0 = 1$. The spectrum for the case with $S = 0.1$ and $\Gamma/\nu_0 = 20$ is multiplied by the factor 0.05 (notation "x0.05" in the figure legend). For both figures, a detector time window of $\Delta T\nu_0 = 5$ was used.

of the single-electron consideration,[9] or Γ (see Fig. 7(b)). The latter is due to the fact that the form of the radiative damping term [cf. Eqs. (5)–(7)] is nonlinear in momentum, so that the oscillations become anharmonic when this term is large enough and strongly influences the dynamics at the time scale $\Delta t \sim 1/\nu_0$. Interestingly, we see from Fig. 7(b) that a drastic increase of the radiative damping constant Γ leads only to a very small blue frequency shift. This is in contrast to the influence of the relaxation parameter γ.

IV. CONCLUSION

To summarize, we have studied the radiative damping effect on the electron dynamics in a Smith-Purcell type graphene-based device and shown that the radiative damping not only contributes to the electron relaxation but is also crucial for the synchronization of their oscillatory motion and, therefore, for an effective coherent emission of the radiation. We have illustrated this for a graphene-based terahertz emitter. The synchronization time depends dramatically on the ratio of the applied dc electric field to the electron scattering rate. Too small values of this ratio lead to the dominance of the dissipation over the input of energy provided by the dc electric field so that the electron oscillations decay rapidly and the coherent emission is suppressed. However, one should keep in mind that large values of this ratio lead to long synchronization times and might also prohibit an effective terahertz emission. Physically, it means that there is an optimal range of dc electric field values for observation of the synchronization of collective electronic motion and coherent emission. The increase of the radiative damping rate leads to the increase of the emission power until it saturates and results in a pronounced anharmonicity of the current oscillations, which manifests itself through enhanced higher harmonics in the emission spectra.

ACKNOWLEDGMENTS

The authors thank Geoffrey Nash, Jerome Faist, Peter Kaspersen, Isaac Luxmoore, and Peter Geiser for useful discussions. The research leading to these results has received funding from the Deutsche Forschungsgemeinschaft and the European Community's Seventh Framework Programme FP7/2007–2013 (Project GOSFEL, Project No. 296391).

APPENDIX: THE RADIATIVE DAMPING TERM IN THE EQUATIONS OF MOTION

The motion of the ith electron under the action of the applied dc field E_0 and the periodic potential $U(x)$ is governed by Eq. (5), where the self-consistent electric field $E_{ac}(t)$, created by all N moving electrons, is related to the two-dimensional current density $j_x(t)$. To find this relationship, we solve the Maxwell equations expanding the fields and currents in Fourier integral

$$E_x(z,t) = \int_{-\infty}^{\infty} d\omega E_x^{\omega}(z) e^{-i\omega t}. \tag{A1}$$

Then, the Fourier components of the electric and magnetic fields, $E_x^{\omega}(z)$ and $B_y^{\omega}(z)$, and of the electric current j_x^{ω} satisfy the following equations:

$$\frac{\partial E_x^{\omega}(z)}{\partial z} - i\frac{\omega}{c} B_y^{\omega}(z) = 0, \tag{A2}$$

$$\frac{\partial B_y^{\omega}(z)}{\partial z} - i\frac{\omega}{c} E_x^{\omega}(z) = -\frac{4\pi}{c} j_x^{\omega}\delta(z). \tag{A3}$$

The solution satisfying the conventional boundary conditions at $z = 0$ and $z \to \pm\infty$ has the form

$$\begin{pmatrix} E_x^{\omega}(z) \\ B_y^{\omega}(z) \end{pmatrix} = -\frac{2\pi}{c} j_x^{\omega} \begin{cases} \begin{pmatrix} 1 \\ 1 \end{pmatrix} e^{i\omega z/c}, & z > 0 \\ \begin{pmatrix} 1 \\ -1 \end{pmatrix} e^{-i\omega z/c}, & z < 0 \end{cases}, \tag{A4}$$

so that at $z = 0$

$$E_x^{\omega}(0) = -\frac{2\pi}{c} j_x^{\omega}. \tag{A5}$$

The solution (A4) and (A5) is valid only at $\omega \neq 0$. If $\omega = 0$, we get from (A2) and (A3)

$$E_x^{\omega=0}(z) = \text{const}, \tag{A6}$$

$$B_y^{\omega=0}(z) = -\frac{2\pi}{c} j_x^{\omega=0} \text{sgn}(z). \tag{A7}$$

The constant magnetic field (A7) does not influence any measured quantity and is of no importance here. The constant dc electric field is already taken into account in Eq. (5) in the term with E_0. The constant in Eq. (A6) can therefore be taken to be zero.

Thus, we get for the Fourier component of the electric field

$$E_x^{\omega}(0) = -\frac{2\pi}{c} j_x^{\omega} \times \begin{cases} 1, & \text{if } \omega \neq 0, \\ 0, & \text{if } \omega = 0. \end{cases} \tag{A8}$$

In this form, there is no dc-current contribution to the radiative damping, as it also should be. However, the field (A8) is discontinuous in one point which leads to a problem. Indeed, substituting (A8) into (A1) and calculating the time-dependent field $E_x(0,t)$ we see that the information about $E_x^{\omega=0}(0) = 0$ is lost.

This problem has arisen since we consider an idealized situation of an infinitely long sample. In reality, the length of the sample L (in the x-direction) is finite, and the Fourier component of the ac electric field vanishes not at the only one point $\omega = 0$, Eq. (A8), but effectively in the range $|\omega| \lesssim \gamma_L$, where γ_L is given by Eq. (9). Therefore, for a real (finite) system, we assume the following functional dependence of $E_x^{\omega}(0)$ on the Fourier component of the current:

$$E_x^{\omega}(0) = -\frac{2\pi}{c} j_x^{\omega}[1 - r(\omega)]. \tag{A9}$$

The function $r(\omega)$ should be equal to 1 at $\omega = 0$, sufficiently fast tend to zero at $|\omega| \gtrsim \gamma_L$, and should satisfy the causality relation between the charge current and the generated ac electric field in the time domain. As a model expression, we take the function

$$r(\omega) = \frac{1}{1 - i\omega/\gamma_L}, \tag{A10}$$

with a pole in the lower complex half-plane to satisfy the causality condition. Now we can return back to Eq. (5) and calculate the field $E_x(t)$. Performing the Fourier transform (A1) of the function (A9) with the $r(\omega)$ function from (A10), we get Eq. (7) with $\bar{j}_x(t)$ from (8). Equation (8) can be rewritten as an ordinary differential equation

$$\frac{d\bar{j}_x}{dt} = \gamma_L(j_x - \bar{j}_x). \tag{A11}$$

[1] S. J. Smith and E. M. Purcell, Phys. Rev. **92**, 1069 (1953).
[2] D. C. Tsui, E. Gornik, and R. A. Logan, Solid State Commun. **35**, 875 (1980).
[3] K. Hirakawa, K. Yamanaka, M. Grayson, and D. C. Tsui, Appl. Phys. Lett. **67**, 2326 (1995).
[4] T. Otsuji, T. Watanabe, A. E. Moutaouakil, H. Karasawa, T. Komori, A. Satou, T. Suemitsu, M. Suemitsu, E. Sano, W. Knap, and V. Ryzhii, J. Infrared, Millimeter, Terahertz Waves **32**, 629 (2011).
[5] S. A. Mikhailov, Phys. Rev. B **58**, 1517 (1998).
[6] K. S. Novoselov, A. K. Geim, S. V. Morozov, D. Jiang, Y. Zhang, S. V. Dubonos, I. V. Grigorieva, and A. A. Firsov, Science **306**, 666 (2004).
[7] K. S. Novoselov, A. K. Geim, S. V. Morozov, D. Jiang, M. I. Katsnelson, I. V. Grigorieva, S. V. Dubonos, and A. A. Firsov, Nature **438**, 197 (2005).
[8] Y. Zhang, Y.-W. Tan, H. L. Stormer, and P. Kim, Nature **438**, 201 (2005).
[9] S. A. Mikhailov, Phys. Rev. B **87**, 115405 (2013).
[10] S. H. Strogatz, *Nonlinear Dynamics And Chaos: With Applications To Physics, Biology, Chemistry, And Engineering* (Westview Press, Boulder, 2001).
[11] A. Pikovsky, M. Rosenblum, and J. Kurths, *Synchronization: A Universal Concept in Nonlinear Sciences*, Cambridge Nonlinear Science Series (Cambridge University Press, Cambridge, 2003).
[12] A. Arenas, A. Diaz-Guilera, J. Kurths, Y. Moreno, and C. Zhou, Phys. Rep. **469**, 93 (2008).
[13] S. H. Strogatz, Physica D **143**, 1 (2000).
[14] L. Brey and H. A. Fertig, Phys. Rev. B **73**, 235411 (2006).
[15] L. Yang, C.-H. Park, Y.-W. Son, M. L. Cohen, and S. G. Louie, Phys. Rev. Lett. **99**, 186801 (2007).
[16] A. R. Akhmerov and C. W. J. Beenakker, Phys. Rev. B **77**, 085423 (2008).
[17] S. A. Mikhailov and K. Ziegler, J. Phys.: Condens. Matter **20**, 384204 (2008).
[18] N. Krumbholz, K. Gerlach, F. Rutz, M. Koch, R. Piesiewicz, T. Kürner, and D. Mittleman, Appl. Phys. Lett. **88**, 202905 (2006).
[19] I. M. Ternov, Phys. - Usp. **38**, 409 (1995).
[20] In reality, they should possess a certain broadening, whose description requires a more rigorous consideration of the scattering processes, going beyond our molecular dynamics model.
[21] J. H. Eberly and K. Wódkiewicz, J. Opt. Soc. Am. **67**, 1252 (1977).
[22] M. G. Raymer, J. Cooper, H. J. Carmichael, M. Beck, and D. T. Smithey, J. Opt. Soc. Am. B **12**, 1801 (1995).
[23] A. S. Moskalenko and J. Berakdar, Phys. Rev. A **78**, 051804(R) (2008).